PREDICTING FATIGUE CRACK INITIATION IN MILLED AEROSPACE GRADE TI-6AL-4V PARTS USING CPFEM

M. F. Arcidiacono[1*], I. Violatos & S. Rahimi[1]

A Crystal Plasticity Finite Element Method (CPFEM) model is proposed for determining the likelihood of fatigue crack initiation and its sites in an aerospace-grade Ti-6Al-4V machined part. The methodology is based on a digitally reconstructed Electron Backscatter Diffraction (EBSD) microstructural model that incorporates the previous deformation history, the residual stress distribution and the roughness profile which result from milling. The constitutive model employs the Armstrong-Frederick nonlinear formulation and implements microstructure sensitive fatigue initiation parameters. Findings suggest that fatigue initiation is significantly influenced by the surface topology and the pre-existing strain and stress fields. The simulation predicts the formation of persistent slip bands within the deformed microstructure and ratcheting that causes local plastic strain accumulation. The model indicates that at the surface and near-surface regions fatigue initiation is mainly driven by local topography, while orientation becomes more dominant at higher depths.

Keywords: Crystal plasticity, Fatigue initiation parameters, Crack initiation

INTRODUCTION

Titanium and its alloys are characterised by a remarkable set of properties: a high strength-to-density ratio, excellent corrosion resistance and biocompatibility. These characteristics make titanium and its alloys a set of attractive materials for the industry, especially for the aeronautics, astronautics and biomedical fields. Although titanium and its alloys are used in diverse fields, most of its production is for the aerospace industry (Khalloufi et al. [1]). In particular, the most commonly used titanium alloy is the $\alpha + \beta$ Ti-6Al-4V, which has good producibility and an outstanding equilibrium of strength, ductility, and properties resistant to fatigue and fracture (Lütjering and Williams [2]). The Ti-6Al-4V alloy is extensively utilised in various states, including annealed, solution treated, and aged, for the production of critical aerospace components such as the airframe, the compressor blades and discs of the jet engine (Gupta et al. [3], Veiga et al. [4]). A recurrent damage mode of Ti-6Al-4V compressor blades and disks is the fatigue crack initiation and propagation due to high cycle fatigue (HCF). Therefore, understanding the mechanisms by which the fatigue cracks initiate is of relevance to optimise manufacturing processes to minimise component damage.

Experimental results show that the high cycle fatigue behaviour of Ti-6Al-4V depends on the microstructure. Lee et al. [5] assessed a set of bimodal Ti-6Al-4V alloys manufactured through different fabrication methods and found substantial differences in fatigue strength due to the morphology of the phases. Wu et al. [6] conducted a statistical analysis of the experimental data of previous works which indicated that the microstructure of the Ti-6Al-4V alloy exerts a significant

effect on the HCF strength. Their work ranked microstructures strength in the decreasing order of bimodal, lamellar and equiaxed. In their study on bimodal microstructures, Wu et al. concluded that the high-cycle fatigue strength initially increases and then decreases as the volume fraction of primary alpha α_p increases. Additionally, they noted that an increase in the size of the α_p grains leads to a reduction in HCF strength.

Alongside the intrinsic properties of the Ti-6Al-4V alloy and its microstructural characteristics, the fatigue initiation of components made from this material could be influenced by post-processing downstream manufacturing operations. For example, machining processes, which are integral to shaping and finishing aerospace components, can induce surface and subsurface alterations to the material that significantly impact the initiation and propagation of fatigue cracks. Liu et al. [7] reviewed the effect of machined surface integrity on fatigue performance of metal workpieces. The analysis revealed that lowering roughness, inclusions and defects, and increasing compressive residual stresses, is beneficial for fatigue performance. In the review, Liu et al. also stated that work hardening delays nucleation but accelerates propagation. Sun et al. [8] investigated the effect of conventional drilling and helical milling of the fatigue response of Ti-6Al-4V and they found that helical milling results in longer fatigue life. The investigation attributed the fatigue life difference to lower surface roughness and less severe plastic deformation caused by the helical tool.

Multiple modelling attempts have been made to explore fatigue crack initiation by means of the Crystal Plasticity Finite Element Method. Liu et al. [9] studied micro-textured regions of alpha grain aggregates using Electron Backscatter Diffraction (EBSD) and found that crack initiation could occur due to the accumulation of plastic strain on prismatic $\langle a \rangle$ slip systems that form dislocation pile ups and cause stress concentration. Chen et al. [10] investigated the crack initiation mechanism of Ti-6Al-4V in the very high cycle fatigue (VHCF) regime using the CPFEM and found that the model was able to capture stress concentration and plastic accumulation, and that alpha colonies significantly affect the VHCF performance of the material. Dinh et al. [11] modelled the effect of surface roughness on the fatigue behaviour of additively manufactured Ti-6Al-4V based on a fatigue initiation parameter and found good agreement with experimental data using the Smith-Watson-Topper variable.

This work aims to present a methodology for fatigue crack initiation analysis of Ti-6Al-4V, based on EBSD maps, which takes into account the previous deformation history of the component due to a milling process. The mechanical behaviour of the material is represented via a kinematic isotropic hardening crystal plasticity constitutive model which is implemented in the finite element method. The previous strain, residual stresses and roughness is considered in the model and the fatigue initiation is analysed through fatigue initiation parameters in order to provide a deeper understanding of the complex interplay effect of each factor in fatigue initiation.

METHODOLOGY

This sections describes the theoretical basis for the development of a micromechanical simulation of Ti-6Al-4V. The methodology includes the crystal plasticity formulation, the fatigue initiation parameters considered in this work and the integration of material characterisation and computational modelling.

Crystal plasticity model

The initiation of high cycle fatigue cracks is linked to the microstructural characteristics and to the previous manufacturing steps. To evaluate the micromechanical response of Ti-6Al-4V it is proposed to implement the crystal plasticity theory in a finite element model. A user-material subroutine (UMAT) based on a code published by Huang [12] was used to incorporate crystal plasticity in Abaqus FEA. The UMAT updates the stress, the state dependent variables and provides the Jacobian matrix to the finite element solver. This approach is based on the pioneering kinematic theory of Taylor [13], Hill [14] and Rice [15] and it is used to describe the deformation at a crystal level.

The deformation gradient can be decomposed into F^e, an elastic and rotational component associated with the stretching of the crystal lattice and rigid body rotation, and F^p, an inelastic component defined by dislocation slip, as follows:

$$F = F^e \, F^p \tag{1}$$

The velocity gradient can be calculated from the deformation gradient tensor with the following equation:

$$L = \dot{F} \, F^{-1} = D + \Omega \tag{2}$$

In equation (2), the velocity gradient is represented as the sum of the rate of deformation D, which is a symmetric tensor that denotes the stretch, and the antisymmetric tensor Ω, the continuum spin. The velocity gradient can be decomposed into an elastic and a plastic component satisfying:

$$L_p = \dot{F}^p \, F^{p-1} = D^p + \Omega^p = \sum_{\alpha=1}^{N_s} \dot{\gamma}^\alpha \, s^\alpha \otimes n^\alpha \tag{3}$$

Where $\dot{\gamma}^\alpha$ is the slipping rate in each slip system and N_s represents the total number of slip systems. s^α and n^α are directional cosines that represent the slip direction and the normal of the slip plane in the deformed configuration, respectively. Assuming that crystalline slip follows Schmid's law, the resolved shear stress τ in a slip system α can be calculated as follows:

$$\tau = \sigma : (s^\alpha \otimes n^\alpha) \tag{4}$$

Where σ is the Cauchy stress tensor, which can be correlated to $\overset{\triangledown}{\sigma}{}^e$, the elastic component of the Jaumann stress rate, with the following relationship:

$$\overset{\triangledown}{\sigma}{}^e = C : D^e - \sigma(I : D^e) \tag{5}$$

C is the elasticity matrix and I is the second order identity tensor. The determination of the stress increments and the Jacobian matrix depend on the increment of shear strain associated with each slip system. This analysis utilises a power law relationship to calculate the slip rates, building upon the foundational work of Peirce, Asaro, and Needleman [16].

$$\dot{\gamma}^\alpha = \dot{\gamma}_0 \left| \frac{\tau^\alpha - x^\alpha}{g^\alpha} \right|^n sgn(\tau^\alpha - x^\alpha) \tag{6}$$

Where $\dot{\gamma}_0$ is the reference strain rate, τ^α is the resolved shear stress of the slip system α, g^α is the current strength of the slip system which represents a resistance to slip, x^α is denotes a back stress and n is the rate sensitivity exponent. The back stress is integrated to the model to account for the Bauschinger effect, that is, to consider the forces that emerge from dislocation pile-ups and their subsequent redistribution upon load reversal during fatigue. For this work, the Armstrong-Frederick

model (Armstrong [17]) was selected to represent the non-linear kinematic hardening effects during fatigue loading:

$$\dot{x}^\alpha = C\dot{\gamma}^\alpha - Dx^\alpha|\dot{\gamma}^\alpha| \tag{7}$$

C is the kinematic hardening modulus and D determines the decay of the back stress up to a maximum saturated stress. The hardening increment of the slip systems is defined by:

$$\dot{g}^\alpha = \sum_{\alpha=1}^{N_s} h_{\alpha\beta}\,\dot{\gamma}^\beta \tag{8}$$

Where $h_{\alpha\alpha}$ and $h_{\alpha\beta}$ are the self- and latent hardening moduli, respectively, and the summation involves all active slip systems. In the present study, the following expression formulated by Peirce et al. [18] was employed:

$$h_{\alpha\alpha} = h(\gamma) = h_0\left|\frac{h_0\,\gamma}{\tau_s - \tau_0}\right| \tag{9}$$

Where h_0 is the initial hardening modulus, τ_0 is the yield strength, τ_s is the shear stress where large plastic flow initiates (stage I), and γ is the cumulative shear strain as follows:

$$\gamma = \sum_{\alpha=1}^{N_s} \int_0^t |\dot{\gamma}^\alpha|dt$$

The latent hardening is calculated as the product of the self-hardening modulus and a constant q:

$$h_{\alpha\beta} = qh(\gamma) \quad \alpha \neq \beta \tag{10}$$

The calibration of the crystal plasticity parameters was done using a reduced microstructure with 70 grains, which facilitated the iterative adjustment of the values and was compared with the fatigue results of Kurath [19]. The elasticity matrix coefficients were obtained from the work of Mayeur et al. [20], who used generalised plane strain elements for finite element simulations. Therefore, the elasticity constants were C_{11}=162400 MPa, C_{12}=92000 MPa, C_{13}=69000 MPa, C_{33}=180700 MPa and C_{44}=46700 MPa. The rest of the parameters were adjusted based on the studies of Zang et al. [21], Kapoor et al. [22] and Han et al. [23]. Table 1 shows the calibrated crystal plasticity parameters.

TABLE 1   Values of the crystal plasticity calibrated parameters.

Parameter	Basal	Prismatic	First Order Pyramidal	All slip systems
$\dot{\gamma}_0$				0.001
n				50
$h_0\,[MPa]$	339	235	281	
$\tau_s\,[MPa]$	242	215	335	
$\tau_0\,[MPa]$	240	211	330	
C				14500
D				160

Fatigue Initiation Parameters

Analysing the formation of cracks due to cyclic loading requires the definition of mesoscopic parameters that reflect driving forces for crack generation as a function of state variables and material properties. These parameters are usually named as fatigue initiation parameters (FIPs) in the literature and they use physical quantities to stablish zones in the microstructure that are prone to crack initiation.

The experimental work of Wilkinson et al. [24] and Ahmed and Wilkinson [25] with electron channelling contrast imaging showed that persistent slip bands are associated with crack initiation at the single crystal domain. Their research revealed that the nucleation of cracks occurs in slip band planes. Therefore, the accumulated plastic strain can be considered as a FIP (Manonukul and Dunne [26], Cheong and Busso [27] and Dunne et al. [28]) given by:

$$FIP_p = \int_0^t \sqrt{\frac{2}{3} \dot{\boldsymbol{\varepsilon}} : \dot{\boldsymbol{\varepsilon}}} \, dt \tag{11}$$

Equation (11) does not discern the contributions from ratcheting effects and those from reversed cyclic plasticity, as delineated by McDowell and Dunne [29], which may be critical in the context of fatigue. McDowell introduced FIPs that explicitly indicate the roles of directional and reversed plasticity in cyclic fatigue (McDowell [30], McDowell [31]). The Fatemi-Socie FIP (Fatemi and Socie [32]) is intended to represent the transgranular slip band formation with the following expression:

$$FIP_{FS} = \max_{\alpha \in (1,\ldots,N_s)} \left[\frac{\Delta \gamma_{p,max}^\alpha}{2} \left(1 + k \, \langle \frac{\sigma_{n,max}^\alpha}{\sigma_0} \rangle \right) \right] \tag{12}$$

Where $\Delta \gamma_{p,max}^\alpha$ is the maximum shear strain range over a cycle, $\sigma_{n,max}^\alpha$ is the normal stress on the plane of maximum shear strain range, k is a material constant that controls the influence of the normal stress and σ_0 is the macroscale yield strength of the material. The maximum shear strain range over a cycle is calculated as the maximum shear strain increment minus the minimum shear strain increment during a time step in the finite element model.

Integration of Material Characterisation and Computational Modelling

A Ti-6Al-4V sample was extracted from a compressor disk used in an aircraft. A scanning electron microscope (SEM) image that shows the material microstructure can be seen in Figure 1a. Electron Backscatter Diffraction was implemented to obtain orientation data of the sample. The extracted data was pre-processed using MTEX, an open-source MATLAB toolbox to analyse crystallographic textures, to create an image of the EBSD with the average local crystal orientations as it is showed in Figure 1b. Since this work is a preliminary investigation, the mapped microstructural morphology does not correspond to a milled sample but it still digitally represents the milled state of the material.

Geometric and orientation data was exported from the MTEX-created EBSD object. This data served as input for an in-house developed Python script designed to interface with the Abaqus FEA software through its application programming interface (API), in order to import the microstructure as a 2D part. The script employs a geometric algorithm designed to decrease the vertex count of each polygon representing a crystal within the microstructure. This vertex reduction aims to minimise the requisite elements for meshing the microstructure while preserving the essential morphological features. The digital microstructure can be seen in Figure 1c. Additionally, the code modifies the

digitalised microstructure to introduce a roughness profile, which was based on the measurements done by Sneddon et al. [33], who measured longitudinal surface roughness profiles for Ti-6Al-4V samples. For this study, a 2.5 μm R_a roughness profile published by Sneddon was implemented as it is shown in Figure 1d.

The microstructure was meshed in Abaqus FEA with 196560 plane strain triangular elements. Boundary conditions were applied for $x = 0$ $(U_x = UR_y = UR_z = 0)$ and $y = 0$ $(U_y = UR_x = UR_z = 0)$ and a cyclic displacement of 0.8% engineering strain $(R = 0)$ was implemented. The simulation was executed for 5 cycles in order to achieve a steady cyclic state. Littlewood et al. [34] showed that after the initial few cycles of fatigue, both the accumulation of slip and the densities of dislocations progress at nearly steady rates per cycle. The material properties were assigned by parsing the input file with a Python script and adding local orientation properties to each element based on the MTEX EBSD map.
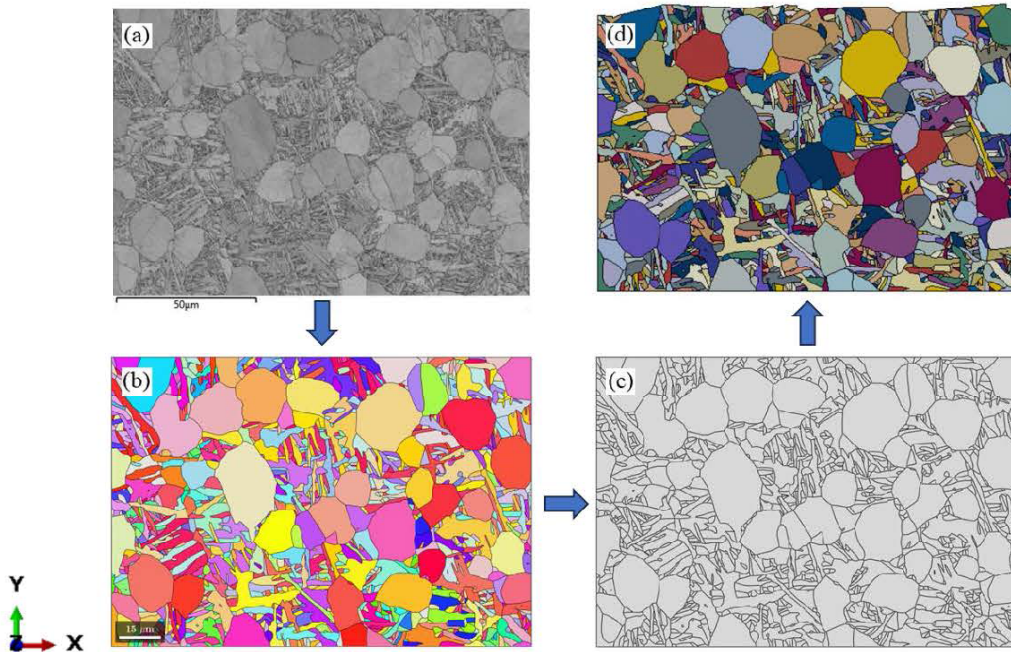

FIGURE 1 (a) Ti-6Al-4V SEM image, (b) MTEX pre-processed image with mean crystal orientation colour map, (c) digital microstructure imported to Abaqus FEA, (d) digital microstructure with roughness profile.

To model the residual stresses, a SIGINI user subroutine was implemented. The SIGINI Fortran code was automatically generated using a Python script that was developed to apply residual stress values as a function of residual stress curves considering the roughness profile. The residual stresses were applied as σ_{xx} and as σ_{zz}, as in-plane and out-of-plane stresses that result from a machining operation. The data of the residual stresses was extracted from the work done by Paranjpe [35], considering the measured stresses induced by flat faced uncoated cutting insert in machined Ti-6Al-4V alloy in flood conditions.

During machining, the near-surface region of a Ti-6Al-4V component experiences plastic deformation. The modelling of this initial strain at a micromechanical level was based on the study

of Brown et al. [36], who compared different conditions of orthogonal cutting and measured the strain by printing a grid using electron beam lithography to measure strain by comparing SEM images of deformed and undeformed grids. The strain was introduced in the crystal plasticity framework by developing a Fortran code that iterates in each integration point up to the strain tensor values as a function of the position of the element. This strategy ensures that the strength, the total cumulative shear strain and the kinematic hardening effect are taken into account from the previous strain history in the fatigue simulation. A flowchart of the computational method is delineated in Figure 2, which provides a visual representation of the process.
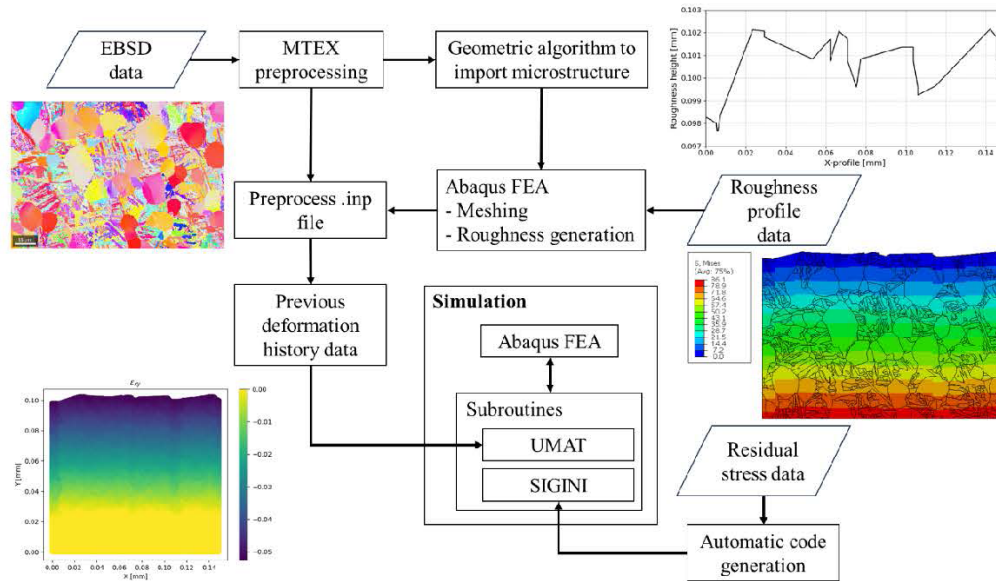

FIGURE 2   Flowchart of the computational method employed to build the simulation.

RESULTS AND DISCUSSION

The computational method employed to create a digital representation of the microstructure depicted in Figure 1 uses an orientation threshold of 7 degrees in the algorithm that defines the grain boundaries, i.e., from Figure 1(a) to Figure 1(b). Additionally, the roughness profile was introduced in the model using the raw data from the profile published by Sneddon et al. [33]. Therefore, it must be noted that there is an inherent uncertainty in capturing particular information from the physical twin and mapping/transferring them into the digital twin for fatigue modelling.

Figure 3(a) shows the predicted Von Mises stress distribution in the microstructure after being subjected to cyclic loading. Von Mises stress was in the range 12 MPa to 1692 MPa, and these maximum and minimum values were located at the machined surface of the material. The stress heterogeneity suggests that the topological features of the surface profile significantly influence the mechanical response of the material.

Figure 3(b) is a magnified region of the surface of Figure 3(a) and it displays the effect of stress concentration due to the surface roughness. The model predicts regions of high stress that arise from the geometric stress concentrators at the surface. It can be observed that stress fields expand and extend towards the subsurface layers of the material and that a field caused by one stress concentration site could link to another field from a different site. The shape of these stress fields is

a function of the surface integrity and the applied load. The simulation presented in this work captures the local orientation effects, including variations inside grains, therefore, the capacity of accommodating strain by the grains results in the final shape of the stress field. The model also predicts regions of low Von Mises stress between stress concentration sites above the high stress fields.
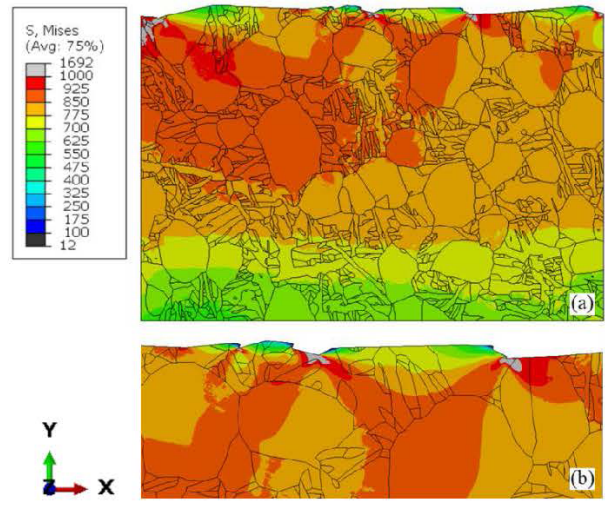

FIGURE 3   (a) Von Mises stress distribution in the digital microstructure. (b) Magnified surface region.
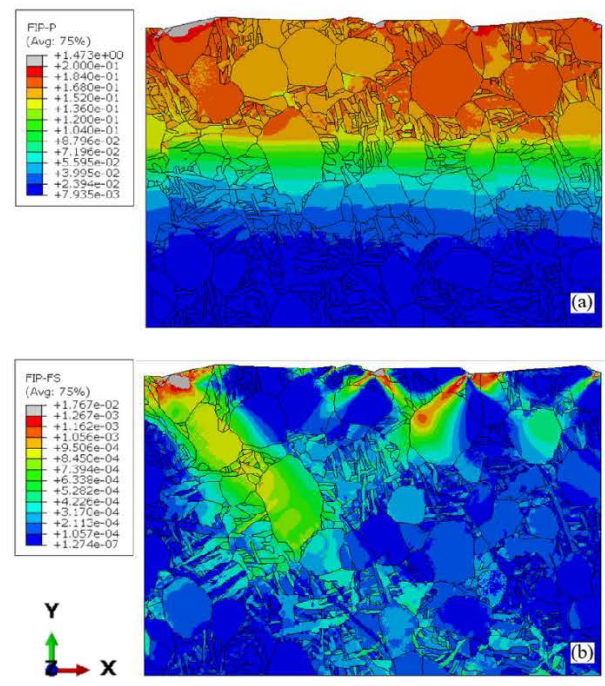

FIGURE 4   (a) Accumulated plastic strain FIP distribution. (b) Fatemi-Socie FIP distribution.

Figure 4(a) shows the accumulated plastic strain fatigue initiation parameter distribution after five cycles. The highest values of the distribution are near the surface and the FIP_p values tend to decrease with depth. Stress concentrators due to the roughness profile could cause high near-surface FIP_p. The observed distribution is a consequence of the combined effect of the machining-induced deformation and cyclic loads. The FIP_p does not distinguish between compressive and tensile strains, therefore, a region with a high compressive strain would appear to have a high FIP_p value despite reducing the probability of fatigue crack initiation under engineering applications limits. As a consequence of these observations, a fatigue initiation parameter based on the total accumulated plasticity is not an appropriate parameter to determine fatigue crack initiation sites in machined parts.

Figure 4(b) depicts the FIP_{FS} distribution after the microstructure was subjected to the same level and cycles of fatigue loading. It can be observed that fatigue initiation is controlled by i) topological stress concentration sites at the surface, and ii) plastic and elastic strain fields at the near-surface regions that lead to the accumulation of strain in specific microstructural features based on their activated slip systems. As the depth increases, the model suggests that the local crystallographic orientation and microstructure morphology can affect fatigue crack initiation. FIP_{FS} fields originate from the surface at angles within the range of 33° to 54° with respect to the load direction, i.e. the horizontal axis. The simulation also predicts an inhomogeneous distribution of fatigue crack initiation likelihood in Ti-6Al-4V colonies due to differences in orientation and inside α primary grains due to the development of slip bands.

Figure 5 shows the accumulated plastic strain in the microstructure (weighted average of all integration points) during the fatigue simulation. An approximately constant increment of plastic strain can be observed, though at higher resolution it was evident that this was the combined effect of the accumulation of strain in zones exceeding their yield strength at a local level and ratcheting which is associated with the Baushinger effect.
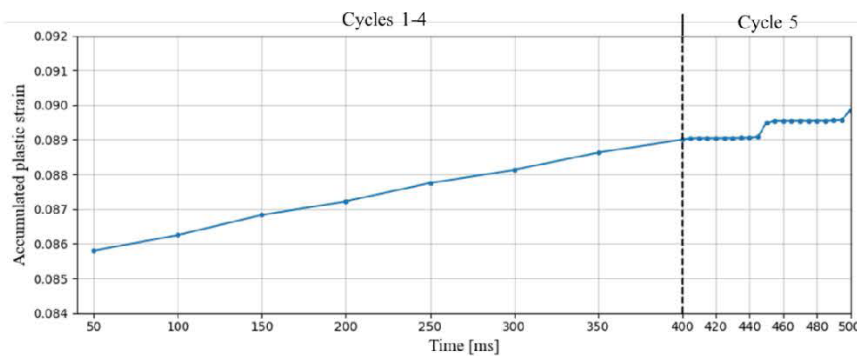

FIGURE 5   Accumulated plastic strain as a function of time during the fatigue simulation.

The model suggests that during the loading and unloading phases of the cycle, plastic strain is accumulated at relatively slow rate, while the upper and bottom limits of the cycle are responsible for a discontinuity in the curve. This result indicates that at the highest value of displacement, some regions are undergoing plastic deformation as they surpass the threshold of the yield surface. When unloading, kinematic hardening effects cause a displacement of the yield surface which also leads to an increase of accumulated plasticity. The non symmetrical behaviour caused by the Bauschinger effect in certain zones of the model produces a ratcheting effect which is associated with high FIP_{FS} values.

CONCLUSION

A novel approach for the prediction of fatigue initiation and its probability distribution was presented for machined parts. The digital reconstruction of the microstructural model consists of a series of steps to integrate experimental data into a crystal plasticity finite element model where machining induced effects were superimposed with EBSD orientation information. The model was subjected to five fatigue cycles which results in the following observations:

1. The surface topology has a significant impact on fatigue initiation due to stress concentration sites that cause plastic strain accumulation and extended stress fields at the surface and at near-surface sites. High stress fields are generated from these sites that link-up and increase the fatigue initiation likelihood in the sub-surface.

2. The total accumulated plastic strain as a fatigue initiation parameter is not appropriate to derive initiation sites when considering previous manufacturing steps and cyclic fatigue loading. The FIP_{FS} formulation is adequate to calculate initiation sites and their likelihood since its expression is a function of the maximum shear strain increment among all slip systems in a cycle.

3. The model indicates that at a surface and near-surface regions, the topology mainly drives fatigue initiation while local microstructure morphology and crystal orientation can contribute to fatigue initiation.

4. The simulation captures ratcheting and predicts that this phenomenon is one of the key drivers of plastic accumulation which could cause fatigue crack initiation.

5. An attempt has been made to take into account the strain history and the initial residual stresses from machining, but their contribution to the response of the material has not been fully investigated or understood.

LIST OF SYMBOLS

F	Deformation gradient	L	Velocity gradient
D	Rate of deformation	Ω	Continuum spin
s^{α}	Slip direction	n^{α}	Slip normal
σ	Cauchy stress	τ	Resolved shear stress
$\overset{\triangledown}{\sigma}$	Jaumann stress rate tensor	C	Elasticity tensor
I	Identity tensor	γ	Shear strain
$\dot{\gamma}^{\alpha}$	Slip rate	g^{α}	Slip system strength
$\dot{\gamma}_0$	Reference strain rate	x^{α}	Back stress
C	Kinematic hardening modulus	D	Kinematic decay coefficient
$h_{\alpha\alpha}$	Self-hardening modulus	$h_{\alpha\beta}$	Latent hardening modulus
q	Latent hardening constant	FIP_p	Accumulated plastic strain
FIP_{FS}	Fatemi-Socie FIP	ε	Strain
t	Time	$\Delta\gamma_p^{\alpha}$	Shear strain range

σ_n^{α}	Normal stress	k	Material constant
σ_0	Yield strength		

REFERENCE LIST

(1) El Khalloufi, M., Drevelle, O., and Soucy, G., *Minerals*, Vol. **11**, No. 12, 2021.

(2) Lütjering, G. and Williams, J. C., *Titanium*, Springer Berlin Heidelberg, Berlin, Germany, 2007.

(3) Gupta, R. K., Kumar, V. A., Mathew, C., and Rao, G. S., *Mater. Sci. Eng. A*, Vol. **662**, 2016, pp. 537–550.

(4) Veiga, C., Davim, J. P., and Loureiro, A. J. R., *Reviews on Advanced Materials Science*, Vol. **32**, No. 2, 2012, pp. 14–34.

(5) Lee, Y. S., Cho, S., Ji, C., Jo, I., and Choi, M., *Metals*, Vol. **12**, No. 10, 2022.

(6) Wu, G. Q., Shi, C. L., Sha, W., Sha, A. X., and Jiang, H. R., *Mater. Des.*, Vol. **46**, 2013, pp. 668–674.

(7) Liu, G., Huang, C., Zhao, B., Wang, W., and Sun, S., *Chin. J. Mech. Eng.*, Vol. **34**, 2021, pp. 1–16.

(8) Sun, D., Keys, D., Jin, Y., Malinov, S., Zhao, Q., and Qin, X., *Procedia CIRP*, Vol. **56**, 2016, pp. 289–292.

(9) Liu, W., Huang, J., Liu, J., Wu, X., Zhang, K., and Huang, A., *Int. J. Fatigue*, Vol. **148**, 2021.

(10) Chen, C., Gao, T., Chen, T., Li, B., Qin, Z., Chen, R., Xue, H., *Eng. Fail. Anal.*, Vol. **152**, 2023.

(11) Dinh, T. D., Han, S., Yaghoubi, V., Xiang, H., Erdelyi, H., Craeghs, T., Segers, J., Van Paepegem, W., *Int. J. Fatigue*, Vol. **144**, no. 106034, 2021.

(12) Huang, Y., *A User-Material Subroutine Incorporating Single Crystal Plasticity in the ABAQUS Finite Element Program*, Harvard University, Report No. MECH-178, 1991.

(13) Taylor, G. I., *J. Inst. Metals*, Vol. **62**, 1938, pp. 307–324.

(14) Hill, R., *J. Mech. Phys. Solids*, Vol. **14**, 1966, pp. 95–102.

(15) Rice, J. R., *J. Mech. Phys. Solids*, Vol. **19**, 1971, pp. 433–455.

(16) Peirce, D., Asaro, R. J., and Needleman, A., Acta Metall., Vol. **31**, No. 12, 1983, pp. 1951–1976.

(17) Armstrong, P.J. and Frederick, C.O., *A mathematical representation of the multiaxial Bauschinger effect*, CEGB, Report RD/B/N731, 1966.

(18) Peirce, D., Asaro, R. J., and Needleman, A., *Acta Metall.*, Vol. **30**, No. 6, 1982, pp. 1087–1119.

(19) Kurath, P., *Final Report: Biaxial Fatigue of Ti-6-4 at 20 ℃*, UIUC, Report No.: UIUC #1-5-521170, 1999.

(20) Mayeur, J. R., McDowell, D. L., and Neu, R. W., *Comput. Mater. Sci.*, Vol. **41**, No. 3, 2008, pp. 356–365.

(21) Zhang, M., Han, F., Tang, B., Kou, H., Fan, J., and Li, J., *J. Mater. Res. Technol.*, Vol. **9**, No. 3, 2020, pp. 5991–6000.

(22) Kapoor, K., Ravi, P., Noraas, R., Park, J. S., Venkatesh, V., and Sangid, M. D., *J. Mech. Phys. Solids*, Vol. **146**, 2021.

(23) Han, F., Tang, B., Kou, H., Li, J., and Feng, Y., *Mater. Sci. Eng. A*, Vol. **625**, 2015, pp. 28–35.

(24) Wilkinson, A. J., Henderson, M. B., and Martin, J. W., *Philos. Mag. Lett.*, Vol. **74**, No. 3, 1996, pp. 145–152.

(25) Ahmed, J., Wilkinson, A. J., and Roberts, S. G., *Philos. Mag. Lett.*, Vol. **76**, No. 4, 1997, pp. 237–246.

(26) Manonukul, A. and Dunne, F. P. E., *Proc. R. Soc. A: Math., Phys. Eng. Sci.*, Vol. **460**, No. 2047, 2004, pp. 1881–1903.

(27) Cheong, K. S. and Busso, E. P., *J. Mech. Phys. Solids*, Vol. **54**, No. 4, 2006, pp. 671–689.

(28) Dunne, F. P. E., Wilkinson, A. J., and Allen, R., *Int. J. Plast.*, Vol. **23**, No. 2, 2007, pp. 273–295.

(29) McDowell, D. L. and F. P. E. Dunne, *Int. J. Fatigue*, Vol. **32**, No. 9, 2010, pp. 1521–1542.

(30) McDowell, D. L., *Mater. Sci. Eng. A*, Vol. **468-470**, 2007, pp. 4–14.

(31) McDowell, D. L., *Fundamentals of Modeling for Metals Processing*, 2009, pp. 408–418.

(32) Fatemi, Ali, and Darrell F. Socie., *Fatigue Fract. Eng. Mater. Struct.*, Vol. **11**, no. 3, 1988, pp. 149–165.

(33) Sneddon, S., Xu, Y., Dixon, M., Rugg, D., Li, P., and Mulvihill, D. M., *Mater. Des.*, Vol. **200**, 2021.

(34) Littlewood, P. D. and Wilkinson, A. J., *Acta Mater.*, Vol. **60**, No. 15, 2012, pp. 5516–5525.

(35) Paranjpe, A., *RESIDUAL STRESSES IN MACHINED TITANIUM (Ti-6Al-4V)*, University of Utah, 2014.

(36) Brown, M., M'Saoubi, R., Crawforth, P., Mantle, A., McGourlay, J., and Ghadbeigi, H., *J. Mater. Process Technol.*, Vol. **299**, 2022.